Hexanematic crossover in epithelial monolayers depends on cell adhesion and cell density

Julia Eckert[1], Benoît Ladoux[2], Luca Giomi[3] and Thomas Schmidt[1*]

[1]Physics of Life Processes, Leiden Institute of Physics, Universiteit Leiden, 2333 CC Leiden, The Netherlands.
[2]Université Paris Cité, CNRS, Institut Jacques Monod, F-75013 Paris, France.
[3]Instituut-Lorentz, Leiden Institute of Physics, Universiteit Leiden, P.O. Box 9506, 2300 RA Leiden, The Netherlands.

*Corresponding author(s). E-mail(s): schmidt@physics.leidenuniv.nl;
Contributing authors: eckert@physics.leidenuniv.nl; benoit.ladoux@ijm.fr; giomi@lorentz.leidenuniv.nl;

Abstract

During tissue folding in developmental processes and monolayer migration in wound healing, epithelial cells undergo shape changes and move collectively. Recent experimental and numerical results suggested that these processes could leverage on the existence of both nematic (2–fold) and hexatic (6–fold) orientational order coexisting at different length scales within the same epithelial layer. Yet, how this remarkable example of multiscale organization in living matter is affected by the material properties of the cells and their substrate is presently unknown. In the current article, we experimentally address these questions in monolayers of Madin-Darby canine kidney cells (MDCK-II) having various cell density and molecular repertoire. At small length scales, confluent monolayers are characterized by a prominent hexatic order and nearly vanishing nematic order, independently on the presence of E-cadherin, the monolayer density, and the underlying substrate stiffness. All three properties, however, dramatically affect the organization of MDCK-II monolayers at large length scales, where nematic order becomes dominant over hexatic order. In particular, we find that the length scale at which nematic order prevails over hexatic order – here referred to as *hexanematic* crossover scale – strongly depends on cell-cell adhesions and correlates with the monolayer density. Our analysis sheds light on how the organization of epithelial layers is affected by the material and mechanical properties, and provides a robust approach for analyzing the tissue composition towards understanding developmental processes.

Keywords: Tissue symmetry, Epithelia, Topological defects, Cell shape index

Introduction

The collective behavior of cells drives tissue patterning and folding during gastrulation, and is involved in wound healing and metastasis[1–5]. Such processes rely on the cross-talk between extracellular matrix adhesions and cell-cell connections through cell junction proteins. Any extracellular changes trigger, for example, the recruitment of focal adhesion molecules, the rearrangement of the actin network at the cell-substrate interface and cell cortex, and causes actomyosin contractions within the cell[6–10]. These biochemical processes, in turn, affect the cell's shape and mechanical properties, thereby influencing the cellular organization at larger length scales[3,11,12].

Among the various aspect of multicellular organization, orientational order has recently been identified as essential concept, because of its inherent propensity towards enhancing the coherence of microscopic forces that would be incoherent (randomly oriented) otherwise[13–19]. Elongated cells, such as fibroblasts[13], neurons[14], and potentially any mesenchymal phenotypes, tend, for instance, to align with each other, thereby giving rise to polar[20,21] or nematic[14,15,22–24] phases, whose spatial structure and dynamics facilitate a number of biomechanical processes. These include the onset of organism-wide cellular flows during gastrulation[25], the development of protrusion and tentacles-like features[18,26], or the extrusion of apoptotic cells[15]. By contrast, various epithelial phenotypes form honeycomb-like structures, held together by cadherin-mediated junctions, where cells are confluent, yet able to move by remodeling of the local honeycomb network. Previous numerical studies suggested that, as other two-dimensional assemblies of equally-sized isotropic building blocks, epithelial layers resemble hexatic liquid crystals: anisotropic fluids featuring quasi-long-ranged $6-$fold orientational order[27–29]. More recently, this picture has been further elaborated by experimental[30] and theoretical[31] studies, which indicated that certain epithelial layers feature in fact a unique combination of nematic and hexatic order, with the former being dominant at large and the latter at small length scale. These two types of liquid crystal order crossover at intermediate length scales – corresponding roughly to clusters of a dozen cells for MDCK-II on uncoated glass[30] – where the local hexagonal structure inherited from the shape of individual cells is gradually replaced by the uniaxial arrangement caused by clustering of cells into chain-like assemblies.

It has been speculated that the specific magnitude of such a *hexanematic* crossover scale – hereafter referred to as $R_\times$ – could affect the strategy of epithelial layers with respect to collective migration[31]. Depending on the length scale L at which it is confined, an epithelial layer could select among the different motility modes at its disposal. E.g. metastatic cells invading the extracellular matrix by collectively migrating through micron-sized channels, for which $L \ll R_\times$, are more likely to adopt migration strategies based on intercalation and other remodeling events rooted into small scale hexatic order. Conversely, the organism-wide collective flow observed in morphogenetic process, for which $L \gg R_\times$, could in principle result from the large scale spontaneous flow that is routinely observed in active nematics. But what sets the magnitude of $R_\times$, and how it can be controlled by epithelia in order to accomplish their biological functions is presently unknown.

In this article we address these questions by measuring the hexanematic crossover length scale, $R_\times$, in epithelial and mesenchymal-like MDCK-II layers, for various cell densities and stiffness of the underling substrate. Our analysis indicates that both these properties profoundly influence the hexanematic crossover. We confirmed our prediction that hexatic symmetry overweights nematic symmetry for individual cells in confluent monolayers, independent of the magnitude and ratio of cell-cell and cell-matrix interaction. The hexanematic crossover length scale in epithelia sheets, however, shifts towards shorter length scales by decreasing monolayer density, reduction of the cell-cell interaction, and to a smaller degree reducing the stiffness of the environment. We suggest that the hexanematic crossover length scale adds a phenotypic parameter that discerns whether cellular behavior is individual or collective.

Results

Reduced cell-cell adhesion increases the shape index and decreases the monolayer density

The cell density in confluent epithelial monolayers affects the morphology and the motility of cells therein[32,33]. It has been proposed that changes in cell shape and motility crucially depend on the development of stable cell-cell adhesions, because of their interplay with the cellular contractility[34].

As a starting point, we investigated how the cell shape is affected by the interaction between cells. To this end, we compared the shape of epithelial MDCK type II wild-type (WT) cells with that of mesenchymal-like MDCK-II E-cadherin knock-out cells (E-cad KO)[19]. A reduced level of cell-cell contacts was maintained in MDCK E-cad KO cells through cadherin-6[19]. Both cell lines, MDCK WT and E-cad KO, were cultured for three days, including two days at confluency, on non-coated glass. Subsequently, samples were fixed and immunostained for the tight junction protein ZO-1, which is localized near the apical surface of cells to determine cell boundaries. We thus used the ZO-1 signal to identify the cell vertex positions and reconstructed a polygon of each cell (Fig.1A-B). Using the polygon, we calculated the shape index, p_0, defined as the ratio between a cell's perimeter, P, and the square root of its area, A, $p_0 = P/\sqrt{A}$[35–37], and conventionally used as an indicator of the cell's shape. By averaging over all mean cell shape indices of all monolayers imaged, we identified that MDCK WT cells had a smaller shape index of 4.06 ± 0.07 (mean ± s.d.) compared to MDCK E-cad KO cells with 4.20 ± 0.21 (mean ± s.d.), p-value < 0.0001 (Fig.1C). This observation is in line with the smaller cell aspect ratio for MDCK WT cells compared to MDCK E-cad KO cells that has been reported earlier[19].

When we compared the morphology of the MDCK WT and E-cad KO cell-monolayers, it appeared that MDCK WT cells were more densely packed and approximatively round (Fig.1A), while MDCK E-cad KO cells were larger and elongated (Fig.1B). We then asked whether the density distributions between both cell lines were different, and whether that was reflected in the shape index. To address this questions, we calculated the mean cell-cell distance between neighboring cells as an indicator for the density. By comparing the distributions between both cell lines, we found that MDCK E-cad KO cells, on average, assumed a larger cell-cell distance of $19.9 \pm 1.0\,\mu\text{m}$ (mean ± s.d.), i.e. one cell per $200 \pm 103\ \mu\text{m}^2$, compared to MDCK WT cells of $16.4 \pm 2.1\,\mu\text{m}$ (mean ± s.d.), i.e. one cell per $295 \pm 153\ \mu\text{m}^2$, (Fig.1D). Therefore, it is conceivable that the larger shape index of MDCK E-cad KO cells was caused by the increased cell-cell distance, i.e. decreased monolayer density.

To assess the correlation between the shape index on the monolayer density, we grouped monolayers according to their mean cell-cell distance, R_{cc}, in six ranges (D1-D6 in Fig.1D). Upon increasing the cell-cell distance – thus decreasing the monolayer density – we observed a monotonic increase in the shape index for both cell lines (Fig.1E), thus corroborating previous experimental observations[33]. MDCK E-cad KO cells assumed a significant larger shape index compared to MDCK WT cells at smaller comparable density ranges ($R_{\text{cc}} \leq 20.1\,\mu\text{m}$; D3-D4). For the largest cell-cell distance range measured ($20.1\,\mu\text{m} \leq R_{\text{cc}} < 22.7\,\mu\text{m}$; D5), the mean shape indices for both cell lines were indistinguishable.

Taken together, the mesenchymal-like MDCK E-cad KO cells had an overall larger shape index and a smaller cell density compared to MDCK WT cells. In the same density range, MDCK E-cad KO cells had either a larger or the same shape index compared to MDCK WT cells.

Hexagonality in epithelia increases with density

As previously mentioned, epithelial layers exhibits hexatic order at the small scale, by virtue of the approximate 6−fold symmetry of individual cells. The latter, in turn, is a natural consequence of the fact that, in two dimensions, isotropic particles pack more densely when arranged in a honeycomb lattice. For rigid disks, this mechanism yields the packing fraction $\phi_{\text{honeycomb}} = \pi\sqrt{3}/6 \approx 0.91$, while the remaining fraction, i.e. $1 - \phi_{\text{honeycomb}} \approx 0.09$, is occupied by the gaps in between the disks. Evidently, the same limitation does not exist in the case of deformable particles, as these can fill the gaps by adapting to the hexagonal geometry of their neighborhood, eventually reaching confluency (i.e. $\phi_{\text{confluent}} = 1$). These considerations suggest that the 'hexagonality' of individual epithelial cells would increase with the monolayer density.

To test this hypothesis, we measured the 6−fold shape parameter, γ_6, introduced in Ref.[30] in both, the MDCK WT and the E-cad KO cell line, and compared it with the 2−fold shape parameter, γ_2, for all individual cells (Fig.S1A-B). These two metrics consist of specific instances of a generic p−fold shape parameter, defined in Eq.(1), quantifying the resemblance of an arbitrary polygon to a p−sided regular polygon (or rod for $p = 2$), having the same position and size. Further, we calculated the ensemble average of the shape parameters, $\langle|\gamma_p|\rangle = 1/N\Sigma_n|\gamma_{p,n}|$,

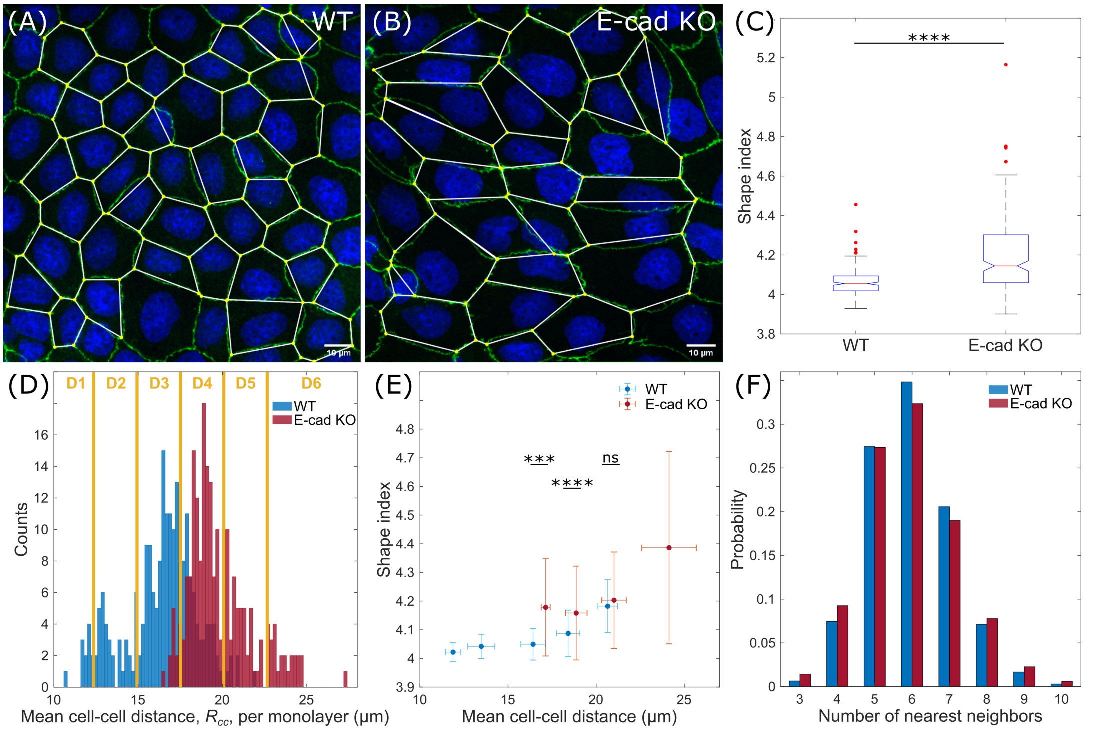

Fig. 1 The cell shape index decreases with increasing monolayer density. (**A,B**), Confocal image of confluent MDCK-II WT and E-cad KO monolayers (green, ZO-1 and blue, nuclei), cultured on non-coated glass. Cells were segmented and their shape reconstructed by connecting the vertices. (**C**) Cell shape index of both cell lines. (**D**), Distribution of the mean cell-cell distance, R_{cc}. The bin-width is 0.2 µm. For further analysis, monolayers were grouped in six ranges, D1-D6, of 2.6 µm-width each ($n_{\text{WT}} = 226$ and $n_{\text{KO}} = 216$ from three independent experiments). (**E**), Mean shape index increases with R_{cc}. (**F**), The probability distribution of the number of nearest neighbors per cell. Error bars represent the standard deviation. Two-sided Wilcoxon rank sum test: *** $p < 0.001$, **** $p < 0.0001$, $^{\text{ns}}$ $p > 0.5$.

where N is the number of all cells of all monolayers. Regardless of the monolayer density and cell line, the mean 6−fold shape parameter was found to be always larger than the 2−fold shape parameter at the scale of individual cells (Fig.2A; Fig.S1A-B). Furthermore, upon increasing cell-cell distance, the difference $\langle|\gamma_6|\rangle - \langle|\gamma_2|\rangle$ decreased (Fig.2B). At the largest cell-cell distance range (D6) of 24.1 ± 1.5 µm (mean ± s.d.), both symmetries were equally prominent, while the difference between MDCK WT and E-cad KO cells disappeared (Fig.2A).

By comparing the individual shape parameters of both MDCK WT and E-cad KO cells in the same monolayer density range, it appeared that the 6−fold shape parameter did not differ in all overlapping density ranges (Fig.2A; p-value > 0.05). On the other hand, the 2−fold shape parameter of MDCK E-cad KO cells were significantly larger for cell-cell distance ranges of $R_{\text{cc}} \leq 20.1$ µm (D3-D4; p-value < 0.0001) and equal in the range of $20.1\,\mu\text{m} \leq R_{\text{cc}} < 22.7\,\mu\text{m}$ (D5; p-value > 0.05) compared to MDCK WT cells. This trend in the behavior of $\langle|\gamma_2|\rangle$ in MDCK WT and E-cad KO cells at similar density ranges echos that observed in the behavior of the shape index (Fig.1E) as also demonstrated by the large correlation between these two parameter (correlation coefficient: $0.93 \leq r \leq 0.97$; see Fig.2C).

From these observations, we concluded that decreasing monolayer density – i.e. increasing cell-cell distance – as well as reducing cell-cell adhesions led to an elongation of cells, which can be equivalently captured by either the cell shape index or the 2−fold shape parameter, γ_2. By contrast, 6−fold symmetry always overweights 2−fold symmetry at the single-cell level, independently on the monolayer density and the strength of cell-cell adhesion. Hence, individual cells in confluent monolayers were statistically more hexagonal rather than elongated.

The absence of E-cadherin shifts the hexanematic crossover towards small length scales

As we anticipated in the Introduction, the 6−fold symmetry characterizing the structure of the cellular network at the length scale of individual cells propagates towards larger length scales, giving rise to hexatic order. The latter decays with distance and is eventually replaced by a similarly decaying nematic order at length scales larger than a system-dependent hexanematic crossover scale $R_\times$. To understand how this depends upon the monolayer mechanical and biochemical properties, we coarse-grained the shape parameters, γ_2 and γ_6, over a disk of radius R, thereby obtaining the scale-dependent shape parameter $\overline{\Gamma}_p = \overline{\Gamma}_p(R)$ (Fig.S1C-D; see Methods for details). In our analysis, R was normalized to the mean cell-cell distance, $R_{\rm cc}$. We then analyzed the behavior of difference $\overline{\Gamma}_6 - \overline{\Gamma}_2$ as a function of the coarse-graining radius and the mean cell-cell distance (Fig.2D-E). In this plot positive (in red) and negative (in blue) $\overline{\Gamma}_6 - \overline{\Gamma}_2$ values correspond respectively to regimes where hexatic order overweights nematic order and vice versa, whereas the white dots mark the hexanematic crossover, where $\overline{\Gamma}_6 = \overline{\Gamma}_2$.

In both MDCK WT (Fig.2D) and E-cad KO cells (Fig.2E), the hexanematic crossover shifted toward smaller and smaller scales upon increasing the cell-cell distance, indicating an increase in the range of hexatic order with the monolayer density. To further highlight this trend, in Fig.2F we plotted the normalized crossover scale $R_\times/R_{\rm cc}$ for each mean cell-cell distance range. In both cell lines, $R_\times/R_{\rm cc}$ decreases approximately linearly with the monolayer density, but with significantly different rate. Specifically, at any given monolayer density, the length scale at which the hexatic order prevailed was more significantly reduced for MDCK E-cad KO in comparison to MDCK WT cells. It is interesting to note that both cell lines could be distinguished more clearly by the relationship between the hexatic-nematic crossover point and the cell-cell distance (Fig.2F), rather than the cell shape index (Fig.1D).

Taken together, our results indicate that the range of hexatic order is larger in MDCK WT cells compared to MDCK E-cad KO cells and increases with the monolayer density. Interestingly, we found that the hexanematic crossover scale provides what appears to be a robust indicator to distinguish the two cell lines.

Multiscale hexanematic order strengthen with the monolayer density

As in molecular liquid crystals, orientational order can be locally disrupted by topological defects, point-like singularity where the cells' local orientation is undefined. In multicellular systems, topological defects are believed to serve various kind of biological functionalities, from driving collective motion at length scales significantly larger than that of individual cells [14,24], to facilitate the extrusion of apoptotic cells [15], and the development of sharp features, such as tentacles and protrusions [26,38].

To shed light on the occurrence of topological defects in our cell layers, we computed the nematic and hexatic orientation fields of MDCK WT and E-cad KO cells and determined the location of the corresponding elementary defects (see Methods for details about the defect tracking method). For each cell-cell distance range and coarse-graining radius, we then computed the corresponding defect density, defined as the number of defects per 100 cells in a monolayer, independently of the cell size. This analysis is shown in Figs.3A and 3B, where the density of nematic defects in MDCK WT and E-cad KO cells, respectively, is plotted against the coarse-graining radius and the mean cell-cell distance. Because the smoothing of the orientation field progressively neutralizes pairs of defects and anti-defects, the overall defect density naturally decreases upon coarse-graining (Fig.S2A-B). Surprisingly, however, the defect density appeared unaffected by the cell-cell distance (Fig.S2C-D for hexatic). In other words, the same number of cells features the same number of defects, independently of their density.

Since nematic and hexatic order occurs in epithelial layers at different length scales, we next investigated how the abundance of nematic and hexatic defects at the crossover scale, where both types of orientational order are simultaneously present. The abundance is shown in Fig.3A-B, where the white dots mark the location of the hexanematic crossover for increasing cell-cell distance.

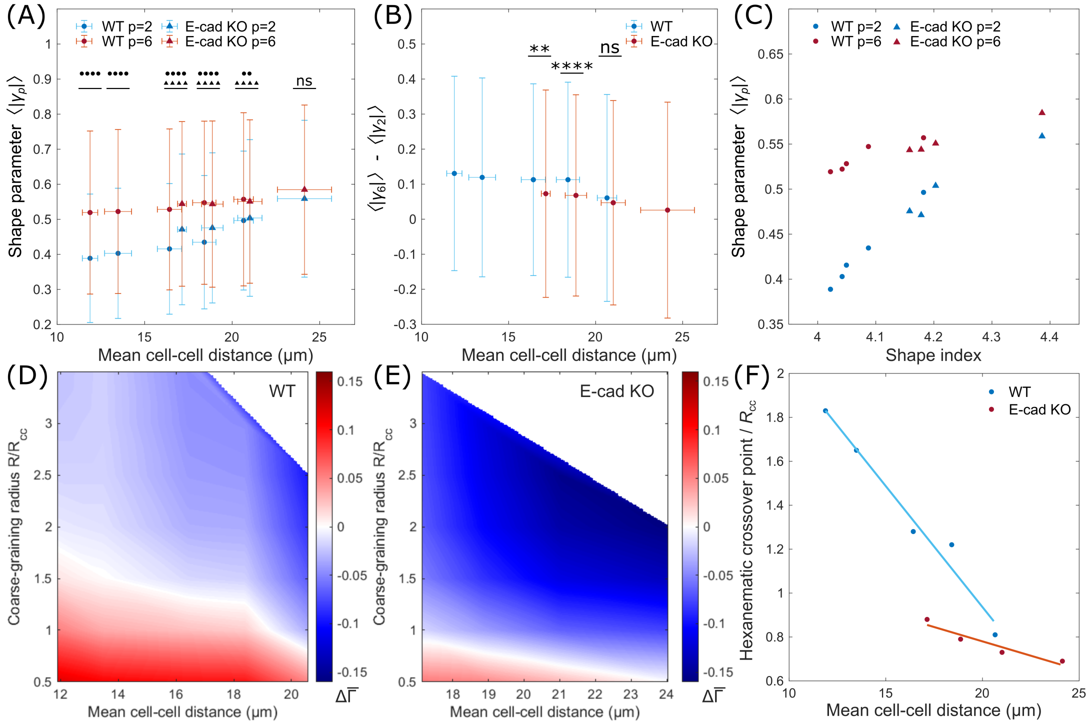

Fig. 2 The dominance and length scale of the hexatic order depends on the monolayer density and cell line. (**A**), The magnitude of the shape parameter, $\langle|\gamma_p|\rangle$, for different mean cell-cell distances. Differences between the hexatic and nematic shape parameters, $\langle|\gamma_6|\rangle - \langle|\gamma_2|\rangle$, are shown in (**B**). (**C**), Correlation between the mean shape index and mean shape parameter. (**D,E**), The difference between the scale-dependent hexatic and nematic shape parameter, $\Delta\overline{\Gamma} = \overline{\Gamma}_6 - \overline{\Gamma}_2$, plotted as a function of the coarse-graining radius and the mean cell-cell distance for MDCK-II WT **(D)** and E-cad KO cells **(E)**. Regions in red and blue indicate the dominance of the hexatic and nematic order, respectively. The white line corresponds to the crossover point, in which both orders are equally represented, $\overline{\Gamma}_6 = \overline{\Gamma}_2$. Individual plots can be seen in Fig.S1C-D. (**F**), Hexanematic crossover points versus the mean cell-cell distance. Error bars represent the standard deviation. Two-sided Wilcoxon rank sum test: ** $p < 0.01$, **** $p < 0.0001$, $^{ns}p > 0.5$.

Upon computing the number of defects at the crossover scale (Fig.3D), we then found that for MDCK WT cells, the nematic and hexatic defects are more abundant in loosely packed monolayers (large cell-cell distance) (Tab.S2). Consistently with the results summarized in the previous sections, this trend was more significant in MDCK WT than in MDCK E-cad KO cells (Tab.S2), consistent with the observation that varying the density of MDCK E-cad KO cells has a limited effect on the hexanematic crossover (Fig.2F).

In conclusion, the defect density, when analyzed at the relevant crossover length scale, was lower for compact monolayers, increasing with decreasing cell density. Given this finding was observed for both shape parameter suggests that both the nematic and the hexatic order together control the collective organization of cells in generating topological defects.

Lower substrate stiffnesses reinforce the length scale of the hexatic order driven by cell-matrix and cell-cell adhesions

In the analysis reported so far, we investigated how the biomechanical properties of the cells – their density and mutual adhesion – affect the hexanematic crossover. Next we focus on the biomechanical properties of the substrate, in particular its stiffness and adhesion with the cell monolayer. To this end, we cultured both cell lines for two days on fibronectin-coated polyacrylamide (PAA) gels of varying stiffness.

On stiff glass substrates, our measurements of the shape index, p_0, (Fig.1E) and the shape parameters, $\langle|\gamma_2|\rangle$ and $\langle|\gamma_6|\rangle$, (Fig.2F), revealed a dependence of the cell shape on monolayer density. The same trend was found on compliant PAA substrates, whose stiffness ranges between 25 kPa and 49 kPa, but with no evidence of a

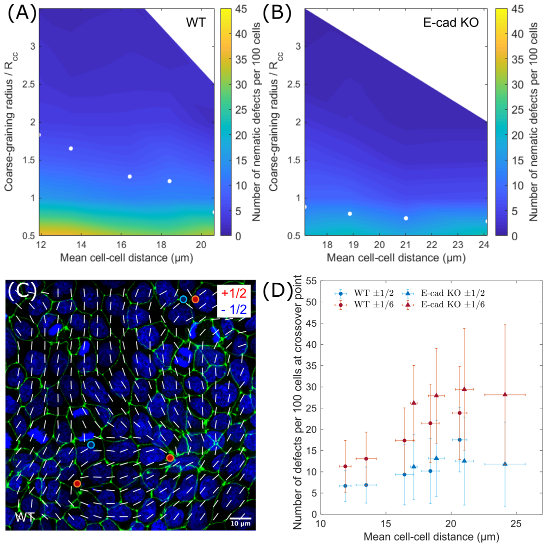

Fig. 3 With equal hexatic and nematic order, the defect density per cell depends on the monolayer density. (**A,B**), The nematic defect density, defined by the number of defects per 100 cells, as a function of the coarse-graining radius and the mean cell-cell distance for MDCK-II WT and E-cad KO cells, respectively. The number of nematic defects created by the same number of cells is independent of the cell density. At the crossover point, represented by white dots, in which the nematic and hexatic orders are equal, the defect density increases with increasing mean cell-cell distance. (**C**), A smooth nematic director field at the crossover point with defects of charge ±1/2. (green, ZO-1 and blue, nuclei) (**D**), The nematic and hexatic defect density formed by MDCK-II WT and E-cad KO cells versus the mean cell-cell distance. Error bars represent the standard deviation.

direct cross-talk between the shape of cells and the stiffness of the substrate. While plated on compliant substrates, cells systematically formed denser monolayers, as demonstrated by the probability distribution of the cell-cell distance (Fig.S3). We then asked whether this change in the monolayer density affected the shape index of cells. For that, we grouped monolayers in the six cell-cell distance ranges (D1-D6; Fig.S3B-C), as above. The shape index of MDCK WT and E-cad KO cells increased with increasing cell-cell distance. However, most of the density ranges showed no significant indication for a stiffness-dependent shape index: by comparing cells on both PAA gels and glass (Fig.4A; Tab.S3), data from MDCK WT and E-cad KO cells overlapped. Consistently with previously reported measurements on epithelial monolayers at jamming[33], our results suggest that, when the cell-cell distance ranges between 9.7 μm and 28.5 μm and substrate stiffness between 25 kPa and 49 kPa, the influence of the monolayer density on the shape index overweights that caused by the stiffness of the substrate.

We next focused on the stiffness-dependence of hexanematic order across length scales. At the scale of individual cells, measurements of the 2−fold and 6−fold shape parameters, $\langle|\gamma_2|\rangle$ and $\langle|\gamma_6|\rangle$, demonstrated a prevalence of 6−fold symmetry irrespective of the cell line, PAA gel stiffness, and monolayer density (Fig.4B-C). On the other hand, analyzing the magnitude of the coarse-grained shape parameters, $|\overline{\Gamma}_2|$ and $|\overline{\Gamma}_6|$, revealed a density-dependence of the hexanematic crossover scale in MDCK WT cells, but not in MDCK E-cad KO cells (Fig.4D). Together with the fact that mesenchymal-like MDCK E-cad KO cells feature higher substrate adhesions and stronger actin stress fibers (Fig.4E-F), reduced intercellular tension, and a lower correlation length in their collective behavior[19], our results suggest that hexatic order could play a role in epithelial phenotypes regardless of the specific properties of the environment.

Discussion

In this article, we explored the multiscale structure of *in vitro* layers of MDCK-II cells, with the goal of unveiling how the mechanical and biochemical properties of the monolayers and the substrate affect the crossover between hexatic and nematic orientational order. Such a remarkable example of multiscale organization in living matter has been recently identified by means of numerical simulations and experiments[30,31], and has been conjectured to contribute to the biophysical versatility of epithelial tissues, whose tasks range from organism-wide morphogenetic migration to collective metastatic invasion under strong confinement.

By comparing the behavior of two different cell lines – MDCK WT and the mesenchymal-like MDCK E-cad KO cells – we showed that the existence of hexatic order crucially relies on E-cadherin-mediated intercellular adhesion, whose lack on MDCK E-cad KO cells rendered the cellular shape significantly elongated, hence prone to form nematic phases. Furthermore, as the lower cell-cell adhesion increases the presence of focal

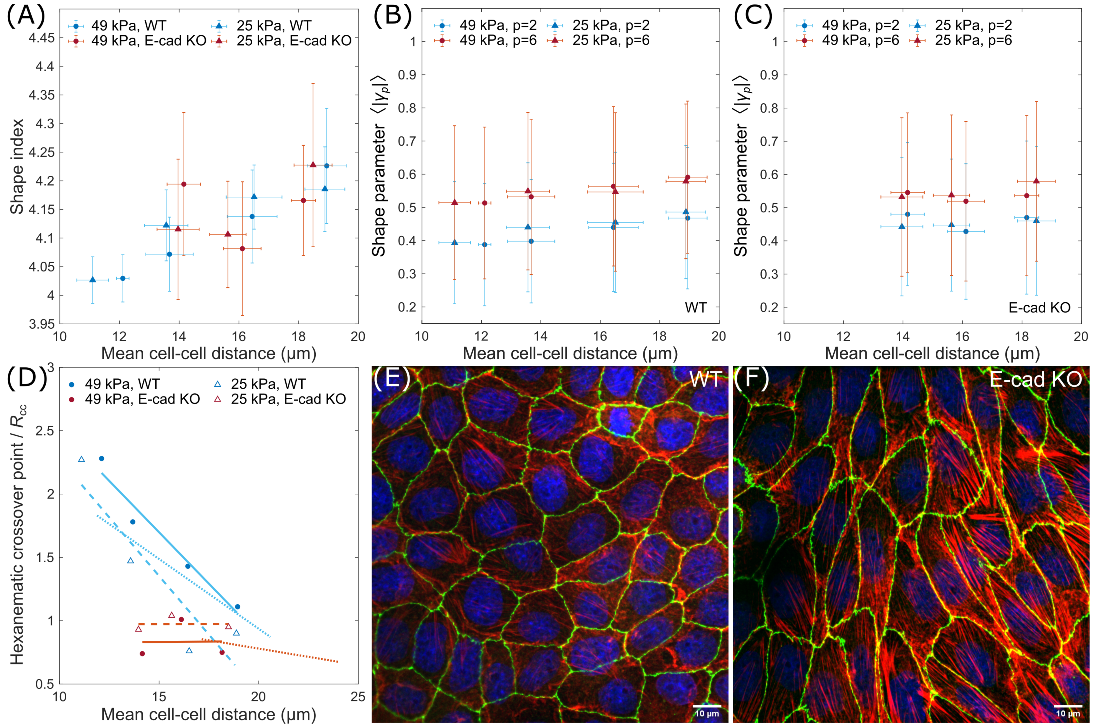

Fig. 4 Substrate stiffness has a minor effect on the hexatic and nematic symmetry. MDCK-II WT and E-cad KO cells were cultured on PAA gels with stiffness of 49 kPa and 25 kPa. (**A**), The mean shape index increases with the mean cell-cell distance, R_{cc}. (**B,C**), On single-cell scale, the mean hexatic shape parameter, $\langle|\gamma_6|\rangle$, always dominants compared to $\langle|\gamma_2|\rangle$. (**D**), The hexanematic crossover points versus the mean cell-cell distance. Independent of PAA stiffness, MDCK-II WT cells show a steeper slope in the crossover point. Dotted lines represent the fits of Fig.2F for cells on non-coated glass. (**E**), MDCK-II WT cells cultured on non-coated glass tend to be roundish and have a less pronounced actin stress fiber network. (**F**), MDCK-II E-cad KO cells cultured on non-coated glass are stretched and show strong F-actin cables (red, F-actin). Error bars represent the standard deviation.

adhesions and actin stress fibers[19] and these contribute to the elongation of the cell[39], we suggest that intercellular- and cell-substrate adhesions jointly control the order of cells in monolayers (see also Ref.[40]). Accordingly, cell-cell adhesion leads to a compact hexagonal shape, whereas actin stress fibers contribute to cell elongation and 2−fold symmetry.

Upon coarse-graining the 2−fold and 6−fold shape parameters, we then identified a significant dependence of the hexanematic crossover on the density of the cell monolayer as well as on the specific cell-line. In MDCK-WT cells, in particular, the hexanematic crossover occurs at larger length scales compared to MDCK E-cad KO cells and the 6−fold symmetry inherited by the shape of individual cells persists up to clusters consisting approximately 3 to 13 cells, depending on the monolayer density. Interestingly, increasing the cell density has been reported to strengthen intercellular adhesion[41,42], while decreasing the alignment of stress fibers[41]. Together with our observations, this suggests that, in epithelial layers, multiple physical and biochemical mechanisms could conspire toward consolidating hexatic order at small length scales. On the other hand, our analysis shows that cell density is an efficient control parameter to manipulate the scale of hexanematic crossover, thus it could possibly be used by the system to switch from a hexatic- to a nematic-based migration mode.

Finally, our data provides a clear demonstration that the specific density-dependence of the hexanematic crossover is not universal, but strongly depends on the cells' molecular repertoire and could be used, in principle, to discern among phenotypes along the epithelial-mesenchymal spectrum.

Methods

Cell culture. MDCK-II WT (ATCC CCL-34) cells and MDCK-II E-cadherin KO cells were cultured in DMEM(1x)+DlutaMax-1 (2340251, Gibcon) supplemented with 10% foetal bovine serum (FBS; Life Technologies) and 1% penicillin/streptomycin (Life Technologies) at 37 °C with 5% CO_2.

Preparation of polyacrylamide gel substrates. Polyacrylamide (PAA) gels were prepared from a stock solution of 40% acrylamide: A (1610140, Bio Rad) and 2% bis-acrylamide: B (1610142, Bio Rad) in PBS. The ratio of these components were mixed according to the PAA gel stiffness of 25.0 ± 2.4 kPa (6/10 total stock volume A, 15/100 total stock volume B) and 49 ± 8 kPa (6/10 total stock volume A, 28/100 total stock volume B), based on the protocol in Ref.[43]. PAA gel stiffnesses were measured using indentation-type atomic force microscopy (Chiaro, Optics11 Life) and interpreted based on the Hertz model. The final PAA solution contained 50/100 total volume stock solution, 5/1000 total volume 10% ammonium persulfate (A3678-25G, Sigma Aldrich) and 15/10,000 total volume TEMED (17919, Thermo Scientific) in PBS. Glass coverslips were plasma activated and incubated with 20 μg ml^{-1} fibronectin (FC010-10MG, Sigma-Aldrich) for 2 h. After incubation, coverslips were rinsed in water to remove excess protein. Simultaneously, a second set of glass coverslips was silanized. Glass coverslips were plasma activated and incubated with a solution of 2% (v/v) 3-(trimethoxysilyl)propyl methacrylate (440159-500ML, Sigma Aldrich) and 1% (v/v) acetic acid (20104.298, VWR Chemicals) in absolute ethanol for 10 min. After rinsing with 96% ethanol, silanized coverslips were heated at 120 °C for 1 h. PAA gels were sandwiched between the fibronectin-coated glass coverslip and silanized coverslip for 20 min. After polymerization, coverslips were separated and samples were kept in water until cell seeding.

Immunostaining. Cells on non-coated coverslips and PAA gels were cultured for three days and two days, respectively, reaching confluence after one to two days. After cell fixation with 4% paraformaldehyde (43368; Alfa Aesar) for 15 min, cells were permeabilized with 0.5% Triton-X 100 for 10 min, blocked with 1% BSA in PBS for 1 h. ZO-1 was visualized with anti-ZO-1 rat monoclonal antibody (1:200 ratio; clone R40.76, MilliporeSigma) followed by staining with Alexa Fluor 488 goat anti-rat (1:200 ratio; A11006, LifeTechnology), F-actin with Alexa Fluor 568 Phalloidin (1:200 ratio; A12380, Invitrogen), and DNA with Hoechst (1:10,000 ratio; 33342 Thermo Fischer).

Imaging. Before imaging, samples were mounted on ProLong (P36962, Invitrogen). Imaging was performed on a microscope setup based on an inverted Axio Observer.Z1 microscope (Zeiss), a Yokogawa CSU-X1 spinning disk, and a 2 ORCA Fusion camera (Hamamatsu). ZEN 2 acquisition software was used for setup-control and data acquisition. Illumination was performed using different lasers (405nm, 488nm, 561nm). Cells were inspected with a 63× 1.4 oil immersion objective (Zeiss). Images were taken in $z-$stack focal-planes with distances of 500 nm for a maximal intensity projection.

Cell shape analysis. *Segmentation.* Cell boundaries of confluent monolayers were analyzed using a maximum intensity projection of $z-$stack images. Cell segmentation and vertex analysis were performed using custom MATLAB scripts (Mathworks, MATLAB R2018a). In short, the ZO-1 signal was thresholded and skeletonized. Branching points shared by at least three cells were identified as vertices. The number of vertices surrounding a cell corresponds to the number of nearest neighbors. To obtain the polygon structure of each cell, vertices were connected by straight lines.

Shape parameter. The shape parameter is defined as a the complex function[30]:

$$\gamma_p = \frac{1}{\Delta_p} \sum_{k=1}^{V} |\boldsymbol{r}_c - \boldsymbol{r}_k|^p e^{ip\phi_k} , \tag{1}$$

where $\boldsymbol{r}_k$ is the position of the $k-$th vertex of the polygon tracing the contour of a cell, $\boldsymbol{r}_c = 1/V \sum_{k=1}^{N} \boldsymbol{r}_k$ is the position of the center of mass, $\Delta_p = \sum_{k=1}^{V} |\boldsymbol{r}_c - \boldsymbol{r}_k|^p$ and $\phi_k = \arctan(y_k/x_k)$ the angular coordinate of the

$k-$th vertex.

Coarse-graining. Coarse-graining was performed over the complex order parameters in Eq. (1) of multiple cells, N_R, inside the disk of radius, $R = (m/2)R_{\text{cc}}$, with $m = 1,\, 2\ldots$:

$$\Gamma_p(R, \boldsymbol{r}_n) = \frac{1}{N_R}\sum_{k=1}^{N_R} \gamma_p\ , \tag{2}$$

where $\boldsymbol{r}_n$ is the position of the disk. Per image, we course-grained at multiple center points, N. The center point of each disk, $\boldsymbol{r}_n$, was set in each lattice point, n, with spacing $R_{\text{cc}}/2$ within a field of view of 124×124 µm. By averaging over all $\Gamma_p(R, \boldsymbol{r}_n)$, we optained the scale-dependent shape parameter:

$$\overline{\Gamma}_p(R) = \frac{1}{N}\sum_{n=1}^{N} |\Gamma_p(R, \boldsymbol{r}_n)|\ . \tag{3}$$

Topological Defects. Topological defects were identified by computing the winding number[44] around a unit cell of a superimposed cartesian grid. The winding number, s, was calculated as

$$s = \frac{1}{2\pi}\sum_{k=1}^{V} (\theta_{k+1} - \theta_k) \bmod \left(\frac{2\pi}{p}\right)\ , \tag{4}$$

where θ is the $p-$fold orientation of the polygon defined from the phase of the shape parameter Γ_p: i.e. $\theta_p = \arctan[\Im(\Gamma_p)/\Re(\Gamma_p)]$.

Statistics. The number of experiments performed and number of images taken are summarized in Tab.S1. All data sets are of non-normal distribution. P-values between two groups were calculated using the two-sided Wilcoxon rank sum test in MATLAB. Comparisons between more than two groups were performed using Dunn's test of multiple comparisons after Kruskal–Wallis significance test in R. Data set significance was defined as of $p \leq 0.05$ (*); $p < 0.01$ (**); $p < 0.001$ (***); $p < 0.0001$ (****); $p > 0.05$ (ns).

Acknowledgments

J.E. acknowledges the EMBO Scientific Exchange Grant (STF reference number: 9076) for financial support to the research visit to Benoît Ladoux's lab at the Institut Jacques Monod in Paris. This work is part of the research program "The Active Matter Physics of Collective Metastasis", project number Science-XL 2019.022, which is financed by the Dutch Research Council (NWO). J.E. acknowledges Wang Xi for the stiffness measurement of the PAA gels, and Josep-Maria Armengol-Collado for the discussions on the theoretical aspects of this work.

Authors' contributions

J.E. conducted and coordinated the research, performed the experiments, and analyzed the data. T.S., B.L. and L.G. supervised the project. All authors conceptualized the results, wrote the manuscript, and agreed on its current version.

Conflict of interest

The authors declare no competing interests.

Supplementary information

Table S1 Number of experiments, samples, imaged monolayers, and analyzed MDCK-II WT and E-cad KO cells on non-coated glass, 25 kPa, and 49 kPa.

		experiments	samples	images	total numner of cells
WT	glass	3	16	226	11987
	25 kPa	5	8	95	9391
	49 kPa	3	6	75	4485
E-cad KO	glass	3	18	216	6941
	25 kPa	3	7	81	5412
	49 kPa	3	11	144	8348

Table S2 Comparison of the defect densities at the crossover point for MDCK-II WT and E-cad KO cells on glass. Cells were classified into groups D1-D6 according to their cell-cell distance. Statistical test: Dunn's test of multiple comparisons after a significant Kruskal–Wallis test. p-value > 0.05, difference is not significantly different.

WT	nematic				hexatic			
p-value	D1	D2	D3	D4	D1	D2	D3	D4
D2	0.50				0.23			
D3	0.17	0.07			0.0037	0.0016		
D4	0.10	0.028	0.23		0.0001	<0.0001	0.008	
D5	0.0024	0.0005	0.0032	0.010	0.0007	0.0010	0.041	0.26

E-cad KO	nematic			hexatic		
p-value	D3	D4	D5	D3	D4	D5
D4	0.20			0.27		
D5	0.33	0.24		0.22	0.34	
D6	0.39	0.23	0.43	0.39	0.35	0.27

Table S3 Comparison of the shape index for MDCK-II WT and E-cad KO cells on glass, 25 kPa and 49 kPa. Cells were classified into groups D1-D6 according to their cell-cell distance. Statistical test: Dunn's test of multiple comparisons after a significant Kruskal–Wallis test. p-value ¿ 0.05, difference is not significantly different.

		WT		E-cad KO	
p-value		glass	25 kPa	glass	25 kPa
25 kPa	D1	0.42			
	D2	0.012			
	D3	0.007		0.28	
	D4	0.012		0.19	
	D5	0.10			
49 kPa	D1	0.49	0.43		
	D2	0.07	0.18		0.005
	D3	0.0015	0.26	0.13	0.29
	D4	0.0001	0.26	0.31	0.38
	D5	0.14	0.37		

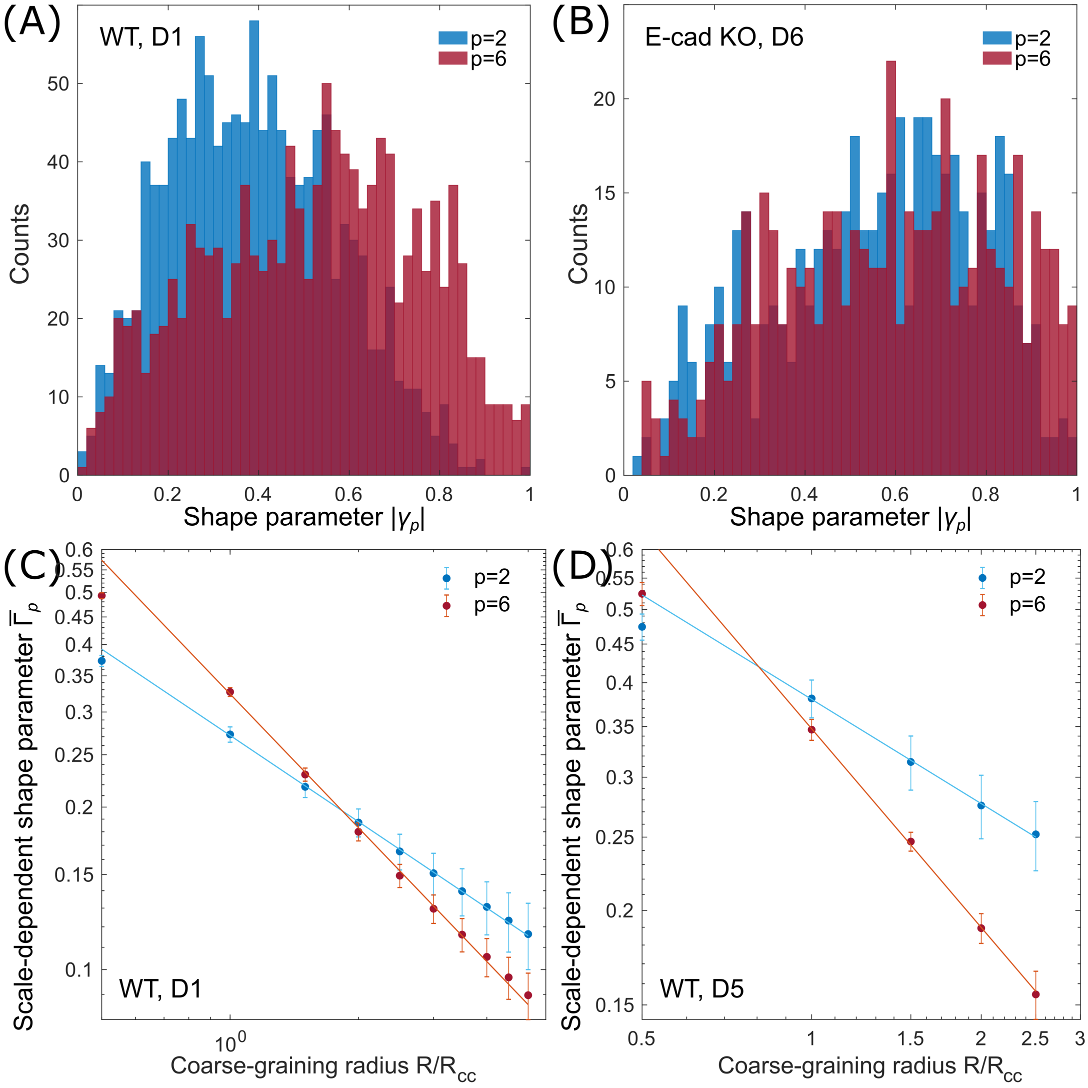

Fig. S1 The nematic and hexatic order depend on the cell line and monolayer density. (**A**,**B**), The magnitude of the cell's shape parameters of all analysed cells within a defined density range. (**A**), For MDCK-II WT cells at a high density range, D1, the distribution of the hexatic shape parameter, $p = 6$, peaks at a higher order compared to the nematic shape parameter, $p = 2$. (**B**), The distributions for the nematic and hexatic shape parameters of MDCK-II E-cad KO cells at a low density range, D6, overlap. (**C**,**D**), The mean of the scale-dependent nematic and hexatic shape parameters, $\overline{\Gamma}_2$ and $\overline{\Gamma}_6$, respectively, of MDCK-II WT cells belonging to different monolayer densities. $\overline{\Gamma}_2$ and $\overline{\Gamma}_6$ decrease by increasing course-graining radius, $R/R_{\rm cc}$. The decrease follows a power law $\overline{\Gamma}_p \sim (R/R_{\rm cc})^{-\eta_p/2}$, with η_p a non-universal exponent. Both fits intersect and define the length scale dependent crossover point from the dominant hexatic to the nematic one. In panel (**C**), the crossover point is at $R/R_{\rm cc} = 1.83$ for cells in the highest density range, D1. This crossover point shifts to a smaller range for lower monolayer densities (**D**), D5, of $R/R_{\rm cc} = 0.81$. A combined plot is shown in Fig.2D-F. Error bars represent the standard error of mean.

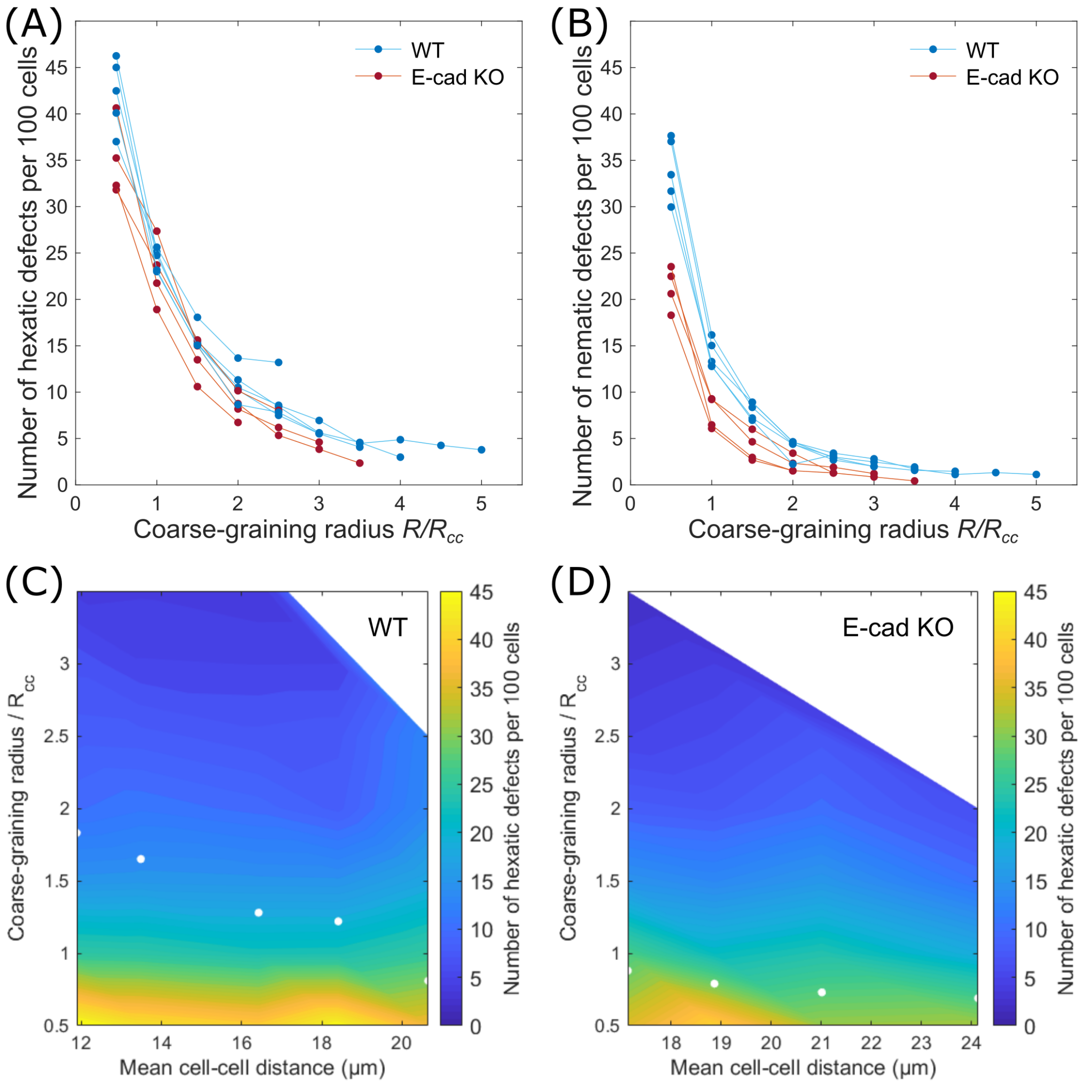

Fig. S2 The defect density depends on the coarse-grained orientation field. (**A,B**), The nematic and hexatic defect density, defined by the number of defects per 100 cells, decreases with increasing coarse-graining radius for MDCK-II WT and E-cad KO cells. (**C,D**), The hexatic defect density as a function of the coarse-graining radius and the mean cell-cell distance for both MDCK-II cell lines.

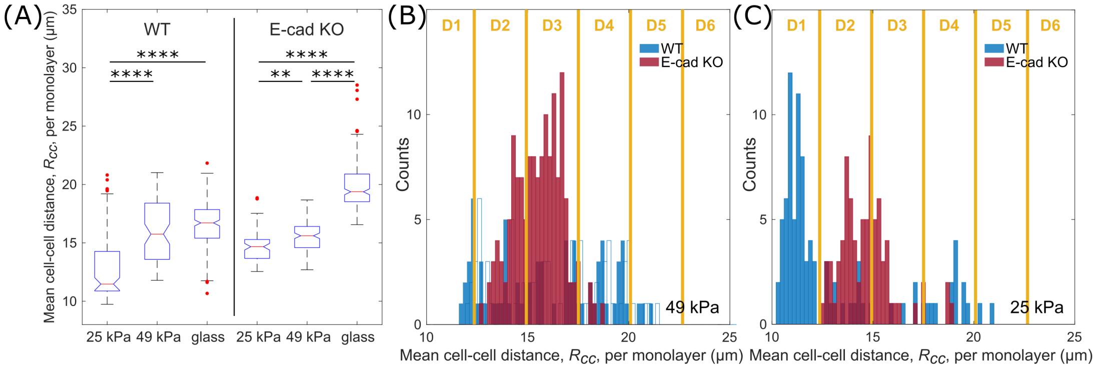

Fig. S3 The mean cell-cell distance increases with increasing substrate stiffness. (**A**), Mean cell-cell distance of nearest neighbors for MDCK-II WT and E-cad KO cells cultured on non-coated glass, and PAA gels with a stiffness of 25 kPa and 49 kPa. Cells tend to be more compact on softer substrates. (**B,C**), Distributions of mean cell-cell distance of both cell lines cultured on 49 kPa and 25 kPa, respectively. Each bin-width is equal to 0.2 μm. For density dependent measurements, cells were grouped in six ranges, D1-D6, of 2.6 μm each (49 kPa: $n_{\mathrm{WT}} = 75$ and n_{KO}=144, 25 kPa: $n_{\mathrm{KO}} = 81$ from three independent experiments; 25 kPa: $n_{\mathrm{WT}} = 95$ from five independent experiments). Comparisons were performed using Dunn's test of multiple comparisons after a significant Kruskal–Wallis test: ** $p < 0.01$; **** $p < 0.0001$.

References

1. T. Lecuit and P.-F. Lenne, “Cell surface mechanics and the control of cell shape, tissue patterns and morphogenesis,” *Nature Reviews Molecular Cell Biology*, vol. 8, no. 8, pp. 633–644, 2007.

2. S. Alt, P. Ganguly, and G. Salbreux, “Vertex models: from cell mechanics to tissue morphogenesis,” *Philosophical transactions of the Royal Society of London. Series B, Biological sciences*, vol. 372, no. 1720, p. 20150520, 2017.

3. C. Guillot and T. Lecuit, “Mechanics of epithelial tissue homeostasis and morphogenesis,” *Science*, vol. 340, no. 6137, pp. 1185–1189, 2013.

4. A. Bailles, C. Collinet, J.-M. Philippe, P.-F. Lenne, E. Munro, and T. Lecuit, “Genetic induction and mechanochemical propagation of a morphogenetic wave,” *Nature*, vol. 572, no. 7770, pp. 467–473, 2019.

5. C. Pérez-González, G. Ceada, F. Greco, M. Matejčić, M. Gómez-González, N. Castro, A. Menendez, S. Kale, D. Krndija, A. G. Clark, V. R. Gannavarapu, A. Álvarez-Varela, P. Roca-Cusachs, E. Batlle, D. M. Vignjevic, M. Arroyo, and X. Trepat, “Mechanical compartmentalization of the intestinal organoid enables crypt folding and collective cell migration,” *Nature Cell Biology*, vol. 23, no. 7, pp. 745–757, 2021.

6. C. Bertet, L. Sulak, and T. Lecuit, “Myosin-dependent junction remodelling controls planar cell intercalation and axis elongation,” *Nature*, vol. 429, no. 6992, pp. 667–671, 2004.

7. G. Salbreux, G. Charras, and E. Paluch, “Actin cortex mechanics and cellular morphogenesis,” *Trends in Cell Biology*, vol. 22, no. 10, pp. 536–545, 2012.

8. C.-P. Heisenberg and Y. Bellaïche, “Forces in tissue morphogenesis and patterning,” *Cell*, vol. 153, no. 5, p. 948962, 2013.

9. S. Gupta, K. Duszyc, S. Verma, S. Budnar, X. Liang, G. A. Gomez, P. Marcq, I. Noordstra, and A. S. Yap, “Enhanced rhoa signalling stabilizes e-cadherin in migrating epithelial monolayers,” *Journal of Cell Science*, vol. 134, no. 17, p. jcs258767, 2021.

10. F. N. Arslan, J. Eckert, T. Schmidt, and C.-P. Heisenberg, “Holding it together: when cadherin meets cadherin,” *Biophysical Journal*, vol. 120, no. 19, pp. 4182–4192, 2021.

11. M. Rauzi, P.-F. Lenne, and T. Lecuit, “Planar polarized actomyosin contractile flows control epithelial junction remodelling,” *Nature*, vol. 468, no. 7327, pp. 1110–1114, 2010.

12. D.-Y. Chen, J. Crest, S. J. Streichan, and D. Bilder, “Extracellular matrix stiffness cues junctional remodeling for 3d tissue elongation,” *Nature Communications*, vol. 10, no. 1, p. 3339, 2019.

13. G. Duclos, C. Erlenkämper, J.-F. Joanny, and P. Silberzan, “Topological defects in confined populations of spindle-shaped cells,” *Nature Physics*, vol. 13, no. 1, pp. 58–62, 2017.
14. K. Kawaguchi, R. Kageyama, and M. Sano, “Topological defects control collective dynamics in neural progenitor cell cultures,” *Nature*, vol. 545, no. 7654, pp. 327–331, 2017.
15. T. B. Saw, A. Doostmohammadi, V. Nier, L. Kocgozlu, S. Thampi, Y. Toyama, P. Marcq, C. T. Lim, J. M. Yeomans, and B. Ladoux, “Topological defects in epithelia govern cell death and extrusion,” *Nature*, vol. 544, no. 7649, pp. 212–216, 2017.
16. T. Turiv, J. Krieger, G. Babakhanova, H. Yu, S. V. Shiyanovskii, Q.-H. Wei, M.-H. Kim, and O. D. Lavrentovich, “Topology control of human fibroblast cells monolayer by liquid crystal elastomer,” *Science Advances*, vol. 6, no. 20, p. eaaz6485, 2020.
17. P. Guillamat, C. Blanch-Mercader, G. Pernollet, K. Kruse, and A. Roux, “Integer topological defects organize stresses driving tissue morphogenesis,” *Nature Materials*, vol. 21, no. 5, pp. 588–597, 2022.
18. Y. Maroudas-Sacks, L. Garion, L. Shani-Zerbib, A. Livshits, E. Braun, and K. Keren, “Topological defects in the nematic order of actin fibres as organization centres of hydra morphogenesis,” *Nature Physics*, vol. 17, no. 2, pp. 251–259, 2021.
19. L. Balasubramaniam, A. Doostmohammadi, T. B. Saw, G. H. N. S. Narayana, R. Mueller, T. Dang, M. Thomas, S. Gupta, S. Sonam, A. S. Yap, Y. Toyama, R.-M. Mège, J. M. Yeomans, and B. Ladoux, “Investigating the nature of active forces in tissues reveals how contractile cells can form extensile monolayers,” *Nature Materials*, vol. 20, p. 1156–1166, 2021.
20. M. Cetera, G. R. Ramirez-San Juan, P. W. Oakes, L. Lewellyn, M. J. Fairchild, G. Tanentzapf, M. L. Gardel, and S. Horne-Badovinac, “Epithelial rotation promotes the global alignment of contractile actin bundles during drosophila egg chamber elongation,” *Nature Communications*, vol. 5, no. 1, p. 5511, 2014.
21. S. Jain, V. M. L. Cachoux, G. H. N. S. Narayana, S. de Beco, J. D’Alessandro, V. Cellerin, T. Chen, M. L. Heuzé, P. Marcq, R.-M. Mège, A. J. Kabla, C. T. Lim, and B. Ladoux, “The role of single-cell mechanical behaviour and polarity in driving collective cell migration,” *Nature Physics*, vol. 16, no. 7, pp. 802–809, 2020.
22. G. Duclos, S. Garcia, H. G. Yevick, and P. Silberzan, “Perfect nematic order in confined monolayers of spindle-shaped cells,” *Soft Matter*, vol. 10, pp. 2346–2353, 2014.
23. T. B. Saw, W. Xi, B. Ladoux, and C. T. Lim, “Biological tissues as active nematic liquid crystals,” *Advanced Materials*, vol. 30, 2018.
24. L. Balasubramaniam, R.-M. Mège, and B. Ladoux, “Active nematics across scales from cytoskeleton organization to tissue morphogenesis,” *Current Opinion in Genetics & Development*, vol. 73, p. 101897, 2022.
25. S. J. Streichan, M. F. Lefebvre, N. Noll, E. F. Wieschaus, and B. I. Shraiman, “Global morphogenetic flow is accurately predicted by the spatial distribution of myosin motors,” *Elife*, vol. 7, p. e27454, 2018.
26. L. A. Hoffmann, L. N. Carenza, J. Eckert, and L. Giomi, “Theory of defect-mediated morphogenesis,” *Science Advances*, vol. 8, no. 15, p. eabk2712, 2022.
27. Y.-W. Li and M. P. Ciamarra, “Role of cell deformability in the two-dimensional melting of biological tissues,” *Phys. Rev. Materials*, vol. 2, p. 045602, 2018.
28. M. Durand and J. Heu, “Thermally driven order-disorder transition in two-dimensional soft cellular systems,” *Phys. Rev. Lett.*, vol. 123, p. 188001, 2019.
29. A. Pasupalak, L. Yan-Wei, R. Ni, and M. Pica Ciamarra, “Hexatic phase in a model of active biological tissues,” *Soft Matter*,

vol. 16, pp. 3914–3920, 2020.

30. J.-M. Armengol-Collado, L. N. Carenza, J. Eckert, D. Krommydas, and L. Giomi, "Epithelia are multiscale active liquid crystals," *arXiv:2202.00668*, 2022.

31. J.-M. Armengol-Collado, L. N. Carenza, and L. Giomi, "Hydrodynamics and multiscale order in confluent epithelia," *arXiv:2202.00651*, 2022.

32. T. E. Angelini, E. Hannezo, X. Trepat, M. Marquez, J. J. Fredberg, and D. A. Weitz, "Glass-like dynamics of collective cell migration," *Proceedings of the National Academy of Sciences*, vol. 108, no. 12, pp. 4714–4719, 2011.

33. J. Devany, D. M. Sussman, T. Yamamoto, M. L. Manning, and M. L. Gardel, "Cell cycle–dependent active stress drives epithelia remodeling," *Proceedings of the National Academy of Sciences*, vol. 118, no. 10, p. e1917853118, 2021.

34. R. Farhadifar, J.-C. Röper, B. Aigouy, S. Eaton, and F. Jülicher, "The influence of cell mechanics, cell-cell interactions, and proliferation on epithelial packing," *Current Biology*, vol. 17, no. 24, pp. 2095–2104, 2007.

35. D. Bi, J. H. Lopez, J. M. Schwarz, and M. L. Manning, "A density-independent rigidity transition in biological tissues," *Nature Physics*, vol. 11, no. 12, pp. 1074–1079, 2015.

36. D. Bi, X. Yang, M. C. Marchetti, and M. L. Manning, "Motility-driven glass and jamming transitions in biological tissues," *Physical review. X*, vol. 6, no. 2, p. 021011, 2016.

37. J.-A. Park, J. H. Kim, D. Bi, J. A. Mitchel, N. T. Qazvini, K. Tantisira, C. Y. Park, M. McGill, S.-H. Kim, B. Gweon, J. Notbohm, R. Steward Jr, S. Burger, S. H. Randell, A. T. Kho, D. T. Tambe, C. Hardin, S. A. Shore, E. Israel, D. A. Weitz, D. J. Tschumperlin, E. P. Henske, S. T. Weiss, M. L. Manning, J. P. Butler, J. M. Drazen, and J. J. Fredberg, "Unjamming and cell shape in the asthmatic airway epithelium," *Nature Materials*, vol. 14, no. 10, pp. 1040–1048, 2015.

38. Y. Maroudas-Sacks, L. Garion, L. Shani-Zerbib, A. Livshits, E. Braun, and K. Keren, "Topological defects in the nematic order of actin fibres as organization centres of hydra morphogenesis," *Nature Physics*, vol. 17, no. 2, pp. 251–259, 2021.

39. K. Schakenraad, J. Ernst, W. Pomp, E. H. J. Danen, R. M. H. Merks, T. Schmidt, and L. Giomi, "Mechanical interplay between cell shape and actin cytoskeleton organization," *Soft Matter*, vol. 16, pp. 6328–6343, 2020.

40. D. Choi, Z. Gonzalez, S. Y. Ho, A. Bermudez, and N. Y. Lin, "Cell-cell adhesion impacts epithelia response to substrate stiffness: Morphology and gene expression," *Biophysical Journal*, vol. 121, no. 2, pp. 336–346, 2022.

41. A. Saraswathibhatla and J. Notbohm, "Tractions and stress fibers control cell shape and rearrangements in collective cell migration," *Physical Review X*, vol. 10, no. 1, p. 011016, 2020.

42. K. Vazquez, A. Saraswathibhatla, and J. Notbohm, "Effect of substrate stiffness on friction in collective cell migration," *Scientific Reports*, vol. 12, no. 1, p. 2474, 2022.

43. S. V. Plotnikov, B. Sabass, U. S. Schwarz, and C. M. Waterman, "Chapter 20 - high-resolution traction force microscopy," in *Quantitative Imaging in Cell Biology* (J. C. Waters and T. Wittman, eds.), vol. 123 of *Methods in Cell Biology*, pp. 367–394, Academic Press, 2014.

44. D. Huterer and T. Vachaspati, "Distribution of singularities in the cosmic microwave background polarization," *Phys. Rev. D*, vol. 72, p. 043004, 2005.

(A)
WT
10 µm
(B)
E-cad KO
10 µm
(C)
****
Shape index
3.8
4
4.2
4.4
4.6
4.8
5
5.2
WT
E-cad KO
(D)
D1
D2
D3
D4
D5
D6
WT
E-cad KO
Counts
0
2
4
6
8
10
12
14
16
10
15
20
25
Mean cell-cell distance, R_{cc}, per monolayer (µm)
(E)
WT
E-cad KO
***
ns
****
Shape index
3.9
4
4.1
4.2
4.3
4.4
4.5
4.6
4.7
4.8
10
15
20
25
Mean cell-cell distance (µm)
(F)
WT
E-cad KO
Probability
0
0.05
0.1
0.15
0.2
0.25
0.3
3
4
5
6
7
8
9
10
Number of nearest neighbors

(A)
WT p=2
WT p=6
E-cad KO p=2
E-cad KO p=6
ns
Shape parameter ⟨|γ_p|⟩
Mean cell-cell distance (μm)
(B)
WT
E-cad KO
**
****
ns
⟨|γ_6|⟩ - ⟨|γ_2|⟩
Mean cell-cell distance (μm)
(C)
WT p=2
WT p=6
E-cad KO p=2
E-cad KO p=6
Shape parameter ⟨|γ_p|⟩
Shape index
(D)
WT
Coarse-graining radius R/R_cc
Mean cell-cell distance (μm)
ΔΓ̄
(E)
E-cad KO
Coarse-graining radius R/R_cc
Mean cell-cell distance (μm)
ΔΓ̄
(F)
WT
E-cad KO
Hexanematic crossover point / R_cc
Mean cell-cell distance (μm)

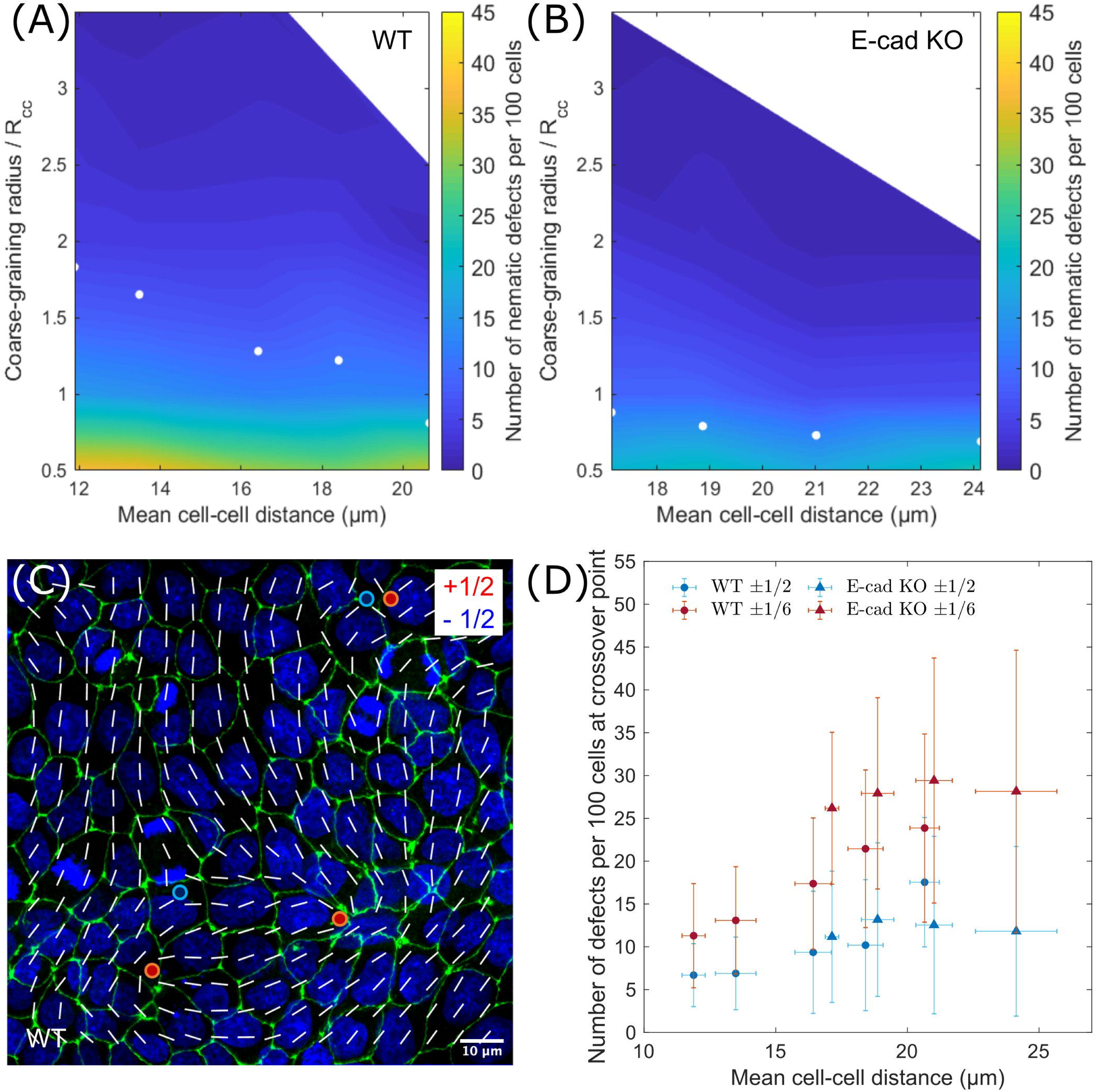
(A)
WT
Coarse-graining radius / R_{cc}
Mean cell-cell distance (μm)
Number of nematic defects per 100 cells
0.5
1
1.5
2
2.5
3
12
14
16
18
20
0
5
10
15
20
25
30
35
40
45
(B)
E-cad KO
Coarse-graining radius / R_{cc}
Mean cell-cell distance (μm)
Number of nematic defects per 100 cells
18
19
20
21
22
23
24
(C)
+1/2
- 1/2
WT
10 μm
(D)
WT ±1/2
WT ±1/6
E-cad KO ±1/2
E-cad KO ±1/6
Number of defects per 100 cells at crossover point
Mean cell-cell distance (μm)
0
5
10
15
20
25
30
35
40
45
50
55
10
15
20
25

(A)
49 kPa, WT
25 kPa, WT
49 kPa, E-cad KO
25 kPa, E-cad KO
Shape index
Mean cell-cell distance (μm)
(B)
49 kPa, p=2
25 kPa, p=2
49 kPa, p=6
25 kPa, p=6
Shape parameter $\langle |\gamma_p| \rangle$
WT
Mean cell-cell distance (μm)
(C)
49 kPa, p=2
25 kPa, p=2
49 kPa, p=6
25 kPa, p=6
Shape parameter $\langle |\gamma_p| \rangle$
E-cad KO
Mean cell-cell distance (μm)
(D)
49 kPa, WT
25 kPa, WT
49 kPa, E-cad KO
25 kPa, E-cad KO
Hexanematic crossover point / R_{cc}
Mean cell-cell distance (μm)
(E)
WT
10 μm
(F)
E-cad KO
10 μm